A Response Spectrum Analysis of Wind Deflection in Railway Overhead Contact Lines Using Pseudo-Excitation Method

Yang Song, *Member, IEEE*, Mingjie Zhang, Hongrui Wang, *Member, IEEE*

***Abstract*—The wind deflection of overhead contact lines (OCLs) challenges the stable and safe operation of electrified railways. The steady wind causes the static deflection of the contact line, while the fluctuating wind leads to the OCL buffeting. This paper performs a response spectrum analysis of the wind deflection caused by the combined effects of steady and fluctuating winds. Considering the initial configuration of OCL, an absolute nodal coordinate formulation method is employed to model the OCL. A spatial wind field including the fluctuating wind in three directions is constructed and the aerodynamic forces on the OCL are derived. A nonlinear solution procedure is proposed to include the geometrical nonlinearity and dropper slackness in the evaluation of static wind deflection. The pseudo-excitation method is utilised to evaluate the buffeting response of the OCL with stochastic wind load. The analysis results indicate that the dropper slackness has a significant effect on the vertical static deflection. Under an extreme wind speed of 40 m/s, the contact line is always within the safe working range of pantograph head when only the steady wind load is considered. However, the stochastic wind load causes non-negligible fluctuation of OCL, and the contact line may be outside of the pantograph working range under the same wind speed. Sensitivity analyses on the effects of some key parameters to the OCL buffeting suggest that the increases of damping ratio and the tension class are effective measures to improve the wind-resistance capability of OCL.**

***Index Terms*—Electrified Railway, Overhead Contact Line, Pantograph Working Length, Wind Deflection, Pseudo-Excitation Method, Buffeting**

I. Introduction

Overhead Contact Line (OCL) constructed along the electrified railway is the only source of power for the electric train. The electric current is normally collected by the locomotive via a pantograph installed on the carbody roof. As shown in Fig. 1, an OCL is comprised of several tensioned cables including the messenger line, contact line and droppers. Due to its long span and large flexibility, the OCL is very sensitive to the wind load, which may cause strong vibration and large deflection of the contact line and threaten the safe and stable operation of the pantograph-OCL system.

Manuscript received xxxx; revised xxxx; accepted xxxx. Date of publication xxxx; date of current version xxxx. The review of this article was coordinated by xxx. (Corresponding author: Mingjie Zhang)

Yang Song and Mingjie Zhang are with the Department of Structural Engineering, Norwegian University of Science and Technology, Trondheim, 7491, Norway. (e-mail: y.song_ac@hotmail.com and mingjie.zhang@ntnu.no).

Hongrui Wang is with the Section of Railway Engineering, Delft University of Technology, 2628CN Deft, The Netherlands (e-mail: soul_wang0@163.com).

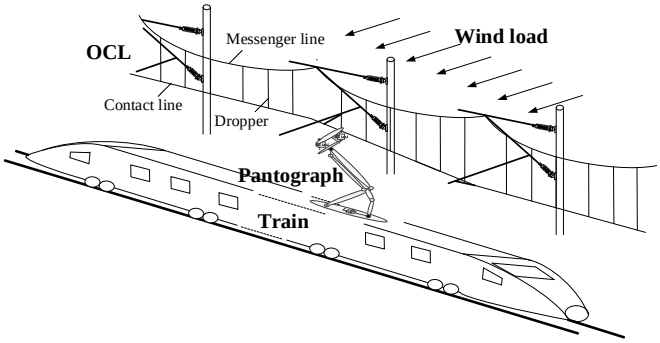

Fig. 1. Schematic of a pantograph-OCL system

A. Problem description

Generally, the environmental wind can be divided into the steady wind and fluctuating wind. They have different effects on long-span structures [1], [2]. Usually the former causes the static deflection of the contact line and the latter results in the forced-vibration (called buffeting) of the OCL. The overlarge lateral deflection of the OCL may cause the contact line to exceed the safety limit of the working range of the pantograph collector, and even lead to the scraping of the pantograph collector and damage the pantograph-OCL system. The strong vertical vibration represents the main source of the incremental contact force fluctuation and the contact loss (namely, the separation of pantograph collector and contact line), which results in frequent arcing and sparking and deteriorates the interaction performance of pantograph-OCL. With the rapid expansion of the high-speed railway industry all over the world, the wind deflection and buffeting of OCL can be frequently observed in some exiting and newly-built high-speed railways, such as the Wuhan-Guangzhou passenger special line and the Beijing-Tianjin inter-city line in China network. The negative effect of wind load (which causes arcing, sparking and even scraping of pantographs) has become a serious issue that limits the trains' maximum operating speed and challenges the safe operation. In order to avoid the overlarge wind deflection of the OCL, the current standard [3] provides a formula to estimate the wind pressure of OCL in the design phase as follows:

$$q_K = \frac{1}{2} G_q G_t \rho V_R^2 \quad (1)$$

in which, G_q is the gust response factor. G_t is the terrain factor taking into account the protection of lines, e.g. in cuts, cities or forest. ρ is the linear density. V_R is the reference wind velocity at a height of 10 m above ground. It is obvious that most coefficients in this formula is selected by experience. The drag and lift coefficients which are essential to determine the aerodynamics of the conductor are not involved in the formula. The OCL normally has a certain lateral displacement (called stagger) to reduce the wear on the pantograph strip. The complex structure of the OCL is not considered in the evaluation of wind deflection in the standard. In addition, the empirical formula does not take the stochastic components of the wind into account, which definitely leads to overly conservative results. As shown in [4], the buffeting of OCL has a significant contribution to the wind deflection, which should not be neglected when evaluating the dynamic performance of OCL.

B. Literature review

In most of the previous studies, a numerical model of OCL is usually used to check the acceptance of the design strategy [5]. In combination with the pantographs' model, various numerical tools have been developed to evaluate the performance of pantograph-OCL interaction system [6]. The contact force between the contact line of the OCL and the registration strip of the pantograph is desired to be stable to ensure a good contact quality [7]. Inadequate contact forces may lead to the contact loss and increase the occurrence of arcing, sparking and contact loss [8], while excessive contact forces cause extra wear of the strip [9] and the contact line [10]. Apart from the contact force, the vibration of OCL is strictly regulated to avoid extra stress and interference with other infrastructures [11], which may cause the failure of OCL components [12]. The accuracy of numerical simulations can be improved by updating the model with field test data [13] and laboratory test data [14]. The previous view of the academic community is that the undesired performance is mainly caused by the uneven distribution of contact line elasticity when the train operates at the conventional speed [15]. However, with the increase of train speed, the wave propagation in the OCL plays an ever-increasing role in affecting the contact quality [16]. The best approach to improve the wave propagation speed is to increase the tension in the OCL. But this is normally restricted by the material limitation [17], [18]. In order to improve the wave propagation property, some parameter optimization methods for OCLs [19], [20] are developed. Some common disturbances such as the locomotive excitations [21] and OCL anomalies [22], [23] are included in the numerical model of OCL to evaluate its contact performance with a pantograph under complex working conditions.

For the study of OCL wind deflection, while galloping may occur under some extreme working conditions [24], [25], buffeting is the most common wind-induced vibration in daily operations. The Buffeting of OCL is analysed in [26]. The time-histories of fluctuating wind velocity in the longitudinal, vertical and lateral directions are generated using empirical spectrums. The stochastic wind loads are exerted on the OCL to evaluate its wind deflection and the wind-induced effects on the pantograph-OCL interaction through a time-domain simulation. However, this work generate a single sequence of the stochastic wind velocity to simulate the wind deflection, which fail to fully represent the stochastic nature of the wind loads. To fully characterize the buffeting response of the OCL under stochastic winds, the Monte Carlos method can be utilised, which is however extremely time-consuming [27]. Meanwhile, the frequency-domain response spectrum method is preferred in buffeting analysis due to its improved computational efficiency [28]. Among various response spectrum methods, the most popular one is the complete quadratic combination (CQC) method [29]. But a significant shortfall of this method is the considerable computational cost. To cope with this issue, the Pseudo-Excitation Method (PEM) is therefore developed in [30] and has been widely used in various industrial backgrounds. This method is adopted in this paper to analyse the OCL buffeting.

C. Contribution of this paper

The main aim of this paper is to evaluate the wind deflection of OCL caused by both of the steady and stochastic winds. A well-recognised OCL model is constructed using a nonlinear finite element method. A shape-finding method is utilised to accurately describe the initial configuration of the OCL. The wind deflection of the OCL is divided in two components. One is the static deflection caused by the steady wind, and the other is the buffeting caused by the fluctuating wind. In this way, the wind deflections of the OCL caused by these two components are evaluated separately. The nonlinearity of the OCL is taken into account to calculate the static deflection induced by the steady wind load. The PEM-based response spectrum analysis is performed to evaluate the displacement standard deviation of the OCL due to the fluctuating wind. The effect of damping ratio and some key structural parameters on the wind deflection is investigated based on a parametric sensitivity analysis.

D. Organisation

The introduction of the background and the literature review is presented in Section I. The finite element formulations of OCL are described in Section II. The aerodynamic force model of OCL is derived in Section III. The evaluation method of wind deflection is described in Section IV. The computational results are presented and analysed in Section V. The effects of some key parameters on the buffeting response are analysed in VI. The conclusions are drawn in Section VII.

II. FINITE ELEMENT MODELLING OF OCL

A nonlinear finite element approach, called the absolute nodal coordinate formulation (ANCF), is adopted to model the OCL. As illustrated in Fig. 2, the ANCF beam is used to model the messenger and contact lines and the steady arm. The dropper wire is modelled by the ANCF cable element without bending degree of freedom (DOF). The claws on clamps of droppers and steady arms are assumed as lumped masses. Here the derivation

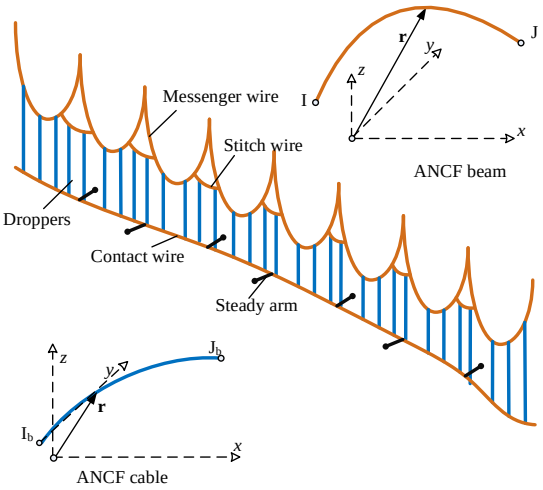

Fig. 2. OCL model based on ANCF beam and cable elements

of the stiffness matrix of ANCF beam element is given as follows. The DOF vector that contains the displacements and the gradients for a beam element is defined by

$$\mathbf{e}=\left[\begin{array}{cccccccccccc} x_i & y_i & z_i & \dfrac{\partial x_i}{\partial \chi} & \dfrac{\partial y_i}{\partial \chi} & \dfrac{\partial z_i}{\partial \chi} & x_j & y_j & z_j & \dfrac{\partial x_j}{\partial \chi} & \dfrac{\partial y_j}{\partial \chi} & \dfrac{\partial z_j}{\partial \chi} \end{array}\right]^{\mathrm{T}} \tag{2}$$

where, χ is the local coordinate in the undeformed configuration ranging from 0 to the element length L_0. The position vector in the deformed configuration $\mathbf{r}$ is interpolated by the shape function matrix $\mathbf{S}$ as

$$\mathbf{r}=\mathbf{Se} \tag{3}$$

in which, $\mathbf{S}$ can be expressed by

$$\mathbf{S}=\left[\begin{array}{cccccccccccc} S_1 & & & S_2 & & & S_3 & & & S_4 & & \\ & S_1 & & & S_2 & & & S_3 & & & S_4 & \\ & & S_1 & & & S_2 & & & S_3 & & & S_4 \end{array}\right]$$

$$\begin{aligned} S_1(\xi)&=1-3\xi^2+2\xi^3 \\ S_2(\xi)&=l_0\left(\xi+\xi^3-2\xi^2\right) \\ S_3(\xi)&=3\xi^2-2\xi^3 \\ S_4(\xi)&=l_0\left(\xi^3-\xi^2\right) \end{aligned} \tag{4}$$

The strain energy U obtained from the contribution of axial and bending deformation can be expressed by

$$U=\frac{1}{2}\int_0^{L_0}(EA\varepsilon_l^2+EI\kappa^2)d\chi \tag{5}$$

in which, E is Young's modulus, A is the section area, I is the moment inertial of the wire, ε_l is the longitudinal strain and κ is the curvature. The generalised elastic forces are calculated by

$$\mathbf{Q}=\left(\frac{\partial U}{\partial \mathbf{e}}\right)^T=\mathbf{K}_e\mathbf{e} \tag{6}$$

Through Eq. (6), the element stiffness matrix $\mathbf{K}_e$ can be obtained. In the shape-finding procedure, the tangent stiffness matrix is typically used to calculate the incremental nodal DOF vector $\Delta\mathbf{e}$ and the incremental unstrained length ΔL_0. The corresponding tangent stiffness matrices $\mathbf{K}_\mathrm{T}$ and $\mathbf{K}_\mathrm{L}$ with respect to $\Delta\mathbf{e}$ and ΔL_0 are derived as follows:

$$\Delta\mathbf{F}=\frac{\partial\mathbf{Q}}{\partial\mathbf{e}}\Delta\mathbf{e}+\frac{\partial\mathbf{Q}}{\partial L_0}\Delta L_0=\mathbf{K}_\mathrm{T}\Delta\mathbf{e}+\mathbf{K}_\mathrm{L}\Delta L_0 \tag{7}$$

Similarly, the tangent stiffness matrices of the ANCF cable element can also be obtained without bending DOFs. It is noted that the ANCF cable element used to model dropper can only withstand tension but not compression. Assembling the element matrices yields the global incremental equilibrium equation for the whole OCL as follows:

$$\Delta\mathbf{F}^\mathrm{G}=\mathbf{K}_\mathrm{T}^\mathrm{G}\Delta\mathbf{U}_\mathrm{C}+\mathbf{K}_\mathrm{L}^\mathrm{G}\Delta\mathbf{L}_0 \tag{8}$$

where $\Delta\mathbf{F}^\mathrm{G}$ is the global unbalanced force vector. $\mathbf{K}_\mathrm{T}^\mathrm{G}$ and $\mathbf{K}_\mathrm{L}^\mathrm{G}$ are the global stiffness matrices related to the incremental nodal displacement vector $\Delta\mathbf{U}_\mathrm{C}$ and the incremental unstrained length vector $\Delta\mathbf{L}_0$, respectively. However, $\left[\mathbf{K}_\mathrm{T}^\mathrm{G}\quad\mathbf{K}_\mathrm{L}^\mathrm{G}\right]$ is not a square matrix. The number of unknowns exceeds the number of equations, which leads to indeterministic solutions. Therefore, additional constraint conditions are provided to restrict undesired movements, according to the design specifications of the OCL.

- The vertical DOFs of dropper points in the contact line are restricted to describe the pre-sag.
- The longitudinal direction of each node is restricted to suppress the undesired movement.
- The tensions are applied to the endpoints of messenger and contact lines.

Introducing the above three types of constraints in Eq. (8), the strained and unstrained lengths of all the elements can be calculated.

Using the reference model in the benchmark [31], a ten-span OCL model is constructed. The initial configuration calculated using the above procedure is presented in Fig. 3. After obtaining the initial configuration of OCL, the global stiffness matrix $\mathbf{K}_\mathrm{T}^\mathrm{G}$ can be obtained at the equilibrium state of the OCL. In combination with a consistent mass matrix $\mathbf{M}_\mathrm{T}^\mathrm{G}$ and damping matrix $\mathbf{C}_\mathrm{T}^\mathrm{G}$, the equation of motion for the OCL excited by external force vector $\mathbf{F}_\mathrm{T}^\mathrm{G}(t)$ can be written by

$$\mathbf{M}_\mathrm{T}^\mathrm{G}\ddot{\mathbf{U}}_\mathrm{C}(t)+\mathbf{C}_\mathrm{T}^\mathrm{G}\dot{\mathbf{U}}_\mathrm{C}(t)+\mathbf{K}_\mathrm{T}^\mathrm{G}(t)\mathbf{U}_\mathrm{C}(t)=\mathbf{F}_\mathrm{T}^\mathrm{G}(t) \tag{9}$$

In the traditional time-domain analysis, Eq. (9) can be solved by a time integration method [32] to obtain the dynamic response of the OCL at each time instant t.

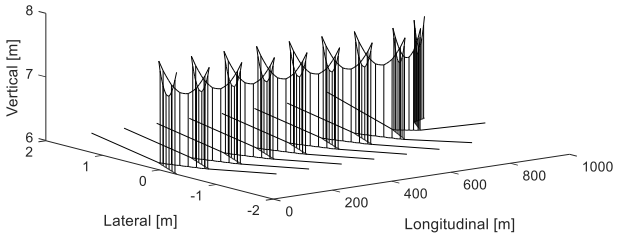

Fig. 3. OCL model based on ANCF beam and cable elements

Table 1. Expressions of empirical spectrum in three directions

Directions	Expressions of empirical spectrum
Along-wind	$S_{\mathrm{u}}(n)=\dfrac{200\,fu_*^2}{n(1+50f)^{5/3}};\ f=\dfrac{nz}{\bar{v}_{\mathrm{s}}}$
Cross-wind	$S_{\mathrm{w}}(n)=\dfrac{13\,fu_*^2}{n(1+20.16f)^{5/3}};\ f=\dfrac{nz}{\bar{v}_{\mathrm{s}}}$
Vertical-wind	$S_{\mathrm{v}}(n)=\dfrac{6\,fu_*^2}{n(1+4f)^{2}};\ f=\dfrac{nz}{\bar{v}_{\mathrm{s}}}$

III. AERODYNAMIC FORCES AND SPECTRA

Assuming that the OCL is only subjected to the wind load, the external force vector $\mathbf{F}_{\mathrm{T}}^{\mathrm{G}}(t)$ contains all the aerodynamic forces on each node. Applying Fourier transform to Eq. (9) yields

$$\left[-\omega^2\mathbf{M}_{\mathrm{T}}^{\mathrm{G}}+i\omega\mathbf{C}_{\mathrm{T}}^{\mathrm{G}}+\mathbf{K}_{\mathrm{T}}^{\mathrm{G}}(\omega)\right]\mathbf{U}_{\mathrm{C}}(\omega)=\mathbf{F}_{\mathrm{T}}^{\mathrm{G}}(\omega) \tag{10}$$

in which, ω is the angular frequency. $\mathbf{U}_{\mathrm{C}}(\omega)$ is the OCL response under the stochastic wind load. In this section, the aerodynamic force vector $\mathbf{F}_{\mathrm{T}}^{\mathrm{G}}(\omega)$ on the right hand is constructed based on the idea of PEM.

A. Stochastic wind spectrums

The stochastic wind is normally decomposed in three components in along-wind, cross-wind and vertical-wind directions. In this section, the Kaimal [33], Panofsky [34] and Tieleman [35] spectrums are adopted to describe the stochastics of fluctuating wind speed in three directions, as shown in Table 1. $\bar{v}_{\mathrm{s}}$ is the steady wind speed. z is the vertical coordinate. n is the frequency. u_* is the friction speed and can be evaluated by

$$u^*=\kappa\bar{v}_{\mathrm{s}}/\ln\left(\frac{z}{z_0}\right) \tag{11}$$

where the Kármán constant κ can be considered to be universal $\kappa=0.4$. z_0 is the roughness length dependant on the roughness of the terrain surface. Mostly the railway is constructed in open areas and a very small value of $z_0=10^{-4}\,\mathrm{m}$ is adopted in this analysis [36].

As the OCL is a long-span structure, the wind speeds at different spatial positions are different. The spatial correlation should be taken into account to generate a spatial wind field. Assuming that the OCL is discretized in N segments, the spectral density function matrix of the fluctuating wind speed in each direction is expressed as follow:

$$\mathbf{S}_{\tau}(n)=\begin{bmatrix} S_{1,1}^{\tau}(n) & \cdots & S_{1,l}^{\tau}(n) & \cdots & S_{1,N}^{\tau}(n)\\ S_{k,1}^{\tau}(n) & \cdots & S_{k,2}^{\tau}(n) & \cdots & S_{k,N}^{\tau}(n)\\ S_{N,1}^{\tau}(n) & \cdots & S_{N,2}^{\tau}(n) & \cdots & S_{N,N}^{\tau}(n)\end{bmatrix} \tag{12}$$

in which, k = 1,2…,N; l = 1,2,…,N; τ can be u, w and v to denotes three stochastic wind directions; When $k=l$, $S_{k,l}^{\tau}(n)$ is the auto-spectrum and $S_{k,l}^{\mathrm{u,v,w}}(n)=S_{\mathrm{u,v,w}}(n)$. When $k\neq l$, $S_{k,l}^{\tau}(n)$ is the cross-spectrum which can be expressed by

$$S_{k,l}^{\mathrm{u,v,w}}(n)=\sqrt{S_{\mathrm{u,v,w}}(n)S_{\mathrm{u,v,w}}(n)}\exp\left\{-\frac{|\omega|\sqrt{C_{x\tau}^2\Delta x^2+C_{y\tau}^2\Delta y^2+C_{z\tau}^2\Delta z^2}}{\pi\bar{v}_{\mathrm{s}}}\right\} \tag{13}$$

where, $C_{x\tau}$, $C_{y\tau}$ and $C_{z\tau}$ are the exponential decay coefficients of the three directions [37].

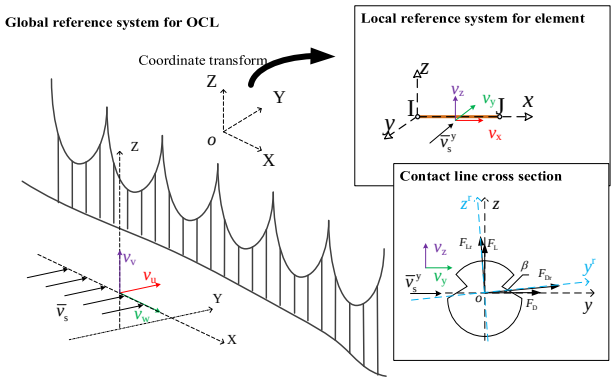

Fig. 4. Schematic of spatial wind field for OCL

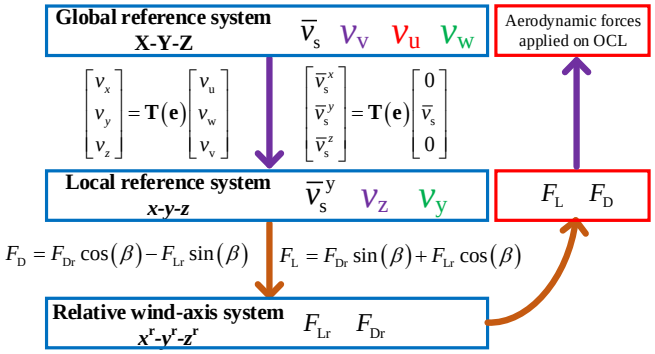

Fig. 5. Relationship among three reference coordinates

B. Aerodynamic forces on contact line

Fig. 4 presents the schematic of the spatial wind field for OCL. Apart from the global reference system, another two main reference systems are defined here to facilitate the derivation. The element local reference system x-y-z is defined by the positions of element node. The relative wind-axis reference system x^{r}-y^{r}-z^{r} is obtained by rotating the x-y-z reference system along the x-axis by β. Here, β is caused by the movement of the contact line subjected to the wind load. The relationship among them is described in Fig. 5. It is seen that the final goal is to obtain the aerodynamic forces applied in the global reference system. Assuming that the OCL is subjected to a crosswind, the steady wind $\bar{v}_{\mathrm{s}}$ is along the Y-axis of the global reference system. The corresponding fluctuating wind components v_{u}, v_{v} and v_{w} are along the Y, X and Z-axis respectively. Due to the existence of stagger, $\bar{v}_{\mathrm{s}}$ is not perpendicular to the cross-section of contact and messenger lines. Therefore, the following coordinate transformation is

performed to transform the wind components to the local reference system for each element.

$$\begin{bmatrix} v_x \\ v_y \\ v_z \end{bmatrix} = \mathbf{T}(\mathbf{e}) \begin{bmatrix} v_{\mathrm{u}} \\ v_{\mathrm{w}} \\ v_{\mathrm{v}} \end{bmatrix}, \quad \begin{bmatrix} \bar{v}_{\mathrm{s}}^{x} \\ \bar{v}_{\mathrm{s}}^{y} \\ \bar{v}_{\mathrm{s}}^{z} \end{bmatrix} = \mathbf{T}(\mathbf{e}) \begin{bmatrix} 0 \\ \bar{v}_{\mathrm{s}} \\ 0 \end{bmatrix} \tag{14}$$

in which, $\mathbf{T}(\mathbf{e})$ is the transformation matrix from global to the local reference system, which is determined by the position of each element. As v_x and $\bar{v}_{\mathrm{s}}^{x}$ are in the longitudinal direction of the element, they have no contribution to the wind deflection. For the fluctuating winds, only v_y and v_z have an effective contribution to the buffeting. For the steady wind, $\bar{v}_{\mathrm{s}}^{z} \approx 0$ if a crosswind is considered. Looking at the contact line cross-section in Fig. 4, the lift F_{L} and drag F_{D} are respectively along the *z* and *y*-axis in element local reference system. In the reference system defined by β, F_{Lr} and F_{Dr} can be expressed by

$$F_{\mathrm{Lr}} = 0.5\rho_{\mathrm{air}} V_{\mathrm{r}} L_{\mathrm{e}} D C_{\mathrm{L}}(\beta) \tag{15a}$$

$$F_{\mathrm{Dr}} = 0.5\rho_{\mathrm{air}} V_{\mathrm{r}} L_{\mathrm{e}} D C_{\mathrm{D}}(\beta) \tag{15b}$$

in which, ρ_{air} is the air density; L_{e} is the length of the contact line element. *D* is the diameter of the contact line cross-section. $C_{\mathrm{L}}(\beta)$ and $C_{\mathrm{D}}(\beta)$ are the lift and drag coefficients at the angle of attack β. V_{r} is the effective wind velocity. So the dynamic wind angle β and the effective wind velocity V_{r} can be expressed by

$$\beta = \arctan\left(\frac{v_z - \dot{z}_{\mathrm{c}}^{\mathrm{r}}}{\bar{v}_{\mathrm{s}}^{y} + v_y - \dot{y}_{\mathrm{c}}^{\mathrm{r}}} \right) \tag{16a}$$

$$V_{\mathrm{r}} = \sqrt{\left(v_z - \dot{z}_{\mathrm{c}}^{\mathrm{r}}\right)^2 + \left(\bar{v}_{\mathrm{s}}^{y} + v_y - \dot{y}_{\mathrm{c}}^{\mathrm{r}}\right)^2} \tag{16b}$$

According to the geometrical relationship, the drag F_{D} and lift F_{L} can be obtained as follows:

$$F_{\mathrm{D}} = F_{\mathrm{Dr}} \cos(\beta) - F_{\mathrm{Lr}} \sin(\beta) \tag{17a}$$

$$F_{\mathrm{L}} = F_{\mathrm{Dr}} \sin(\beta) + F_{\mathrm{Lr}} \cos(\beta) \tag{17b}$$

where $\dot{z}_{\mathrm{c}}^{\mathrm{r}}$ and $\dot{y}_{\mathrm{c}}^{\mathrm{r}}$ are the velocities of the contact line cross-section in the vertical-wind and along-wind directions, which can be calculated by

$$\begin{cases} \dot{y}_{\mathrm{c}}^{\mathrm{r}} = \dot{y}_{\mathrm{c}} \cos\beta + \dot{z}_{\mathrm{c}} \sin\beta \\ \dot{z}_{\mathrm{c}}^{\mathrm{r}} = \dot{z}_{\mathrm{c}} \cos\beta - \dot{y}_{\mathrm{c}} \sin\beta \end{cases} \tag{18}$$

in which $\dot{y}_{\mathrm{c}}$ and $\dot{z}_{\mathrm{c}}$ are the lateral and vertical velocities of contact line cross-section in element local coordinate system. As β is very small, the following assumption can be made:

$$\beta = \arctan\left(\frac{v_z - \dot{z}_{\mathrm{c}}^{\mathrm{r}}}{\bar{v}_{\mathrm{s}}^{y} + v_y - \dot{y}_{\mathrm{c}}^{\mathrm{r}}} \right) \approx \frac{v_z}{\bar{v}_{\mathrm{s}}^{y}} \tag{19a}$$

$$\sin(\beta) \approx \beta; \quad \cos(\beta) = 1 - \beta^2 / 2 \tag{19b}$$

$$C_{\mathrm{L}}(\beta) = C_{\mathrm{L}}(0) + \dot{C}_{\mathrm{L}}(0)\beta \tag{19c}$$

$$C_{\mathrm{D}}(\beta) = C_{\mathrm{D}}(0) + \dot{C}_{\mathrm{D}}(0)\beta \tag{19d}$$

in which, $C_{\mathrm{L}}(0)$ and $C_{\mathrm{D}}(0)$ denote the lift and drag coefficients at the attack angle of 0°. By substituting Eq. (19) and Eq. (15) into Eq. (17) and neglecting high order terms, F_D and F_L can be obtained as

$$F_{\mathrm{D}} = F_{\mathrm{D}}^{\mathrm{bf}} + F_{\mathrm{D}}^{\mathrm{s}} \tag{20a}$$

$$F_{\mathrm{L}} = F_{\mathrm{L}}^{\mathrm{bf}} + F_{\mathrm{L}}^{\mathrm{s}} \tag{20b}$$

in which,

$$F_{\mathrm{D}}^{\mathrm{bf}} = 0.5\rho_{air} \bar{v}_{\mathrm{s}}^{y2} L_{\mathrm{e}} D \left[C_{\mathrm{D}} \bullet \frac{2v_y}{\bar{v}_{\mathrm{s}}^{y}} + \dot{C}_{\mathrm{D}} \bullet \frac{v_z}{\bar{v}_{\mathrm{s}}^{y}} \right] \tag{21a}$$

$$F_{\mathrm{D}}^{\mathrm{s}} = 0.5\,\rho_{air} \bar{v}_{\mathrm{s}}^{y2} D L_{\mathrm{e}} C_{\mathrm{D}} \tag{21b}$$

$$F_{\mathrm{L}}^{\mathrm{bf}} = 0.5\rho_{air} \bar{v}_{\mathrm{s}}^{y2} L_{\mathrm{e}} D \left[C_{\mathrm{L}} \bullet \frac{2v_y}{\bar{v}_{\mathrm{s}}^{y}} + \left(\dot{C}_{\mathrm{L}} + C_{\mathrm{D}} \right) \bullet \frac{v_z}{\bar{v}_{\mathrm{s}}^{y}} \right] \tag{21c}$$

$$F_{\mathrm{L}}^{\mathrm{s}} = 0.5\,\rho_{air} \bar{v}_{\mathrm{s}}^{y2} D L_{\mathrm{e}} C_{\mathrm{L}} \tag{21d}$$

From Eq. (20), it is seen that the aerodynamic forces on the contact line can be considered as the sum of the static force caused by the steady wind and the buffeting force caused by the fluctuating wind. By transferring Eq. (20) to global reference system, the aerodynamic forces can be applied in the equation of motion for OCL to evaluate the wind deflection. The aerodynamic forces on the messenger line and droppers can also be obtained similarly.

IV. Evaluation of Wind Deflection

The wind deflection can be assumed to be the summation of the static wind deflection and the buffeting response. Therefore, the calculation of wind deflection is divided into two parts to evaluate the static wind deflection and the OCL buffeting separately.

A. Static wind deflection

The calculation of static wind deflection is a classic static solution procedure. The static wind load vector $\mathbf{F}_{\mathrm{static}}$ can be generated by assembling Eq. (21b) and (21d). If the OCL nonlinearity (including the geometrical nonlinearity of contact and messenger lines and the slackness of droppers) is not considered, the static wind deflection $\Delta\mathbf{U}_{\mathrm{static}}$ with respect to the initial configuration can be simply evaluated by

$$\Delta\mathbf{U}_{\mathrm{static}} = \left[\mathbf{K}_{\mathrm{T}}^{\mathrm{G}} \right]^{-1} \mathbf{F}_{\mathrm{static}} \tag{22}$$

If the geometrical nonlinearity is considered, Eqs. (7-8) should be adopted and an iteration must be performed to eliminate the unbalanced force. It should be noted that the incremental unstrained length vector . $\Delta\mathbf{L}_0$. should be set to zero. In each iterative step, Eq. (7) is used to calculate the unbalanced force. Eq. (8) is adopted to calculate the incremental displacement. The tangent stiffness matrix $\mathbf{K}_{\mathrm{T}}^{\mathrm{G}}$ is updated in each iteration step according to the displacement of OCL.

B. Pseudo-Excitation Method

The PEM simplifies the classical stochastic vibration problem to the solution of structural random response with a series of harmonic loads [38]. This sub-section describes the application

of PEM to the wind deflection evaluation of OCL with stochastic wind loads.

Normally the frequency of OCL buffeting cannot be very high. Thus, only the first several modes contribute significantly to the buffeting response. Based on this idea, the mode analysis is performed to Eq. (9) to obtain the first q mode shapes and natural frequencies. Therefore the mode function matrix $\mathbf{\Phi}=\left[\phi_1,\phi_2,\cdots\phi_q\right]$ and the natural frequency matrix $\mathbf{\Omega}^2=\mathrm{diag}\left[\omega_1^2,\omega_2^2,\cdots,\omega_q^2\right]$ are obtained.

$$\mathbf{K}_{\mathrm{T}}^{\mathrm{G}}\mathbf{\Phi}=\mathbf{M}_{\mathrm{T}}^{\mathrm{G}}\mathbf{\Phi}\mathbf{\Omega}^2 \tag{23}$$

in which, ϕ_j and ω_j are the j^{th} mode and natural frequency of the OCL, respectively. Eq. (9) can be rewritten as

$$\left[-\omega^2\tilde{\mathbf{M}}_{\mathrm{T}}^{\mathrm{G}}+i\omega\tilde{\mathbf{C}}_{\mathrm{T}}^{\mathrm{G}}+\tilde{\mathbf{K}}_{\mathrm{T}}^{\mathrm{G}}\right]\tilde{\mathbf{U}}_{\mathrm{C}}\left(\omega\right)=\tilde{\mathbf{F}}_{\mathrm{T}}^{\mathrm{G}}\left(\omega\right) \tag{24}$$

in which,

$$\begin{aligned}&\tilde{\mathbf{M}}_{\mathrm{T}}^{\mathrm{G}}=\mathbf{\Phi}^{\mathrm{T}}\mathbf{M}_{\mathrm{T}}^{\mathrm{G}}\mathbf{\Phi},\quad \tilde{\mathbf{C}}_{\mathrm{T}}^{\mathrm{G}}=\mathbf{\Phi}^{\mathrm{T}}\mathbf{C}_{\mathrm{T}}^{\mathrm{G}}\mathbf{\Phi}\\ &\tilde{\mathbf{K}}_{\mathrm{T}}^{\mathrm{G}}=\mathbf{\Phi}^{\mathrm{T}}\mathbf{K}_{\mathrm{T}}^{\mathrm{G}}\mathbf{\Phi},\quad \tilde{\mathbf{U}}_{\mathrm{C}}\left(\omega\right)=\mathbf{\Phi}^{\mathrm{T}}\tilde{\mathbf{U}}_{\mathrm{C}}\left(\omega\right)\\ &\tilde{\mathbf{F}}_{\mathrm{T}}^{\mathrm{G}}\left(\omega\right)=\mathbf{\Phi}^{\mathrm{T}}\mathbf{F}_{\mathrm{T}}^{\mathrm{G}}\left(\omega\right)\end{aligned} \tag{25}$$

In Eq. (24), $\tilde{\mathbf{M}}_{\mathrm{T}}^{\mathrm{G}}$, $\tilde{\mathbf{C}}_{\mathrm{T}}^{\mathrm{G}}$ and $\tilde{\mathbf{K}}_{\mathrm{T}}^{\mathrm{G}}$ are all diagonal matrices. So the equation can be decomposed into q independent equations and solved separately.

The aerodynamic excitation on the right hand of Eq. (10) can be generated by

$$\mathbf{F}_{\mathrm{T}}^{\mathrm{G}}\left(\omega\right)=\mathbf{R}p\left(\omega\right) \tag{26}$$

in which $p\left(\omega\right)$ is the random excitation vector in the frequency domain. $\mathbf{R}$ is the matrix describing the distribution of excitation. For the buffeting problem, the spectral excitation matrix $\mathbf{S}_{\mathrm{FF}}\left(\omega\right)$ of $p\left(\omega\right)$ can be derived by

$$\mathbf{S}_{\mathrm{FF}}\left(\omega\right)=\mathbf{Q}\mathbf{S}_{\mathrm{u,v,w}}\left(\omega\right)\mathbf{Q}^{\mathrm{T}} \tag{27}$$

where $\mathbf{Q}$ is the transformation matrix from fluctuating wind velocities to aerodynamic forces, which can be generated according to the derivation in Section III. To facilitate the generation of the pseudo-excitation vector in PEM, the Cholesky decomposition is applied to $\mathbf{S}_{\mathrm{FF}}(\omega)$ and yields

$$\mathbf{S}_{\mathrm{FF}}(\omega)=\mathbf{L}^{*}\mathbf{d}\,\mathbf{L}^{\mathrm{T}} \tag{28}$$

where $\mathbf{L}$ is a lower triangular matrix with unity as its diagonal elements. $\mathbf{d}$ is a diagonal matrix with d_r as its rth diagonal element. Physically, $\sqrt{d_r}\mathbf{L}_r\mathrm{e}^{i\omega t}$ can be taken as the harmonic generalised pseudo-excitation for Eq. (10), in which $\mathbf{L}_r$ is the rth column of $\mathbf{L}$. Looking at the jth mode, the equation of motion can be written as

$$\ddot{\eta}_{r,j}+2\omega_j\xi_j\dot{\eta}_{r,j}+\omega_j^2\eta_{r,j}=\frac{\phi_j^{\mathrm{T}}\mathbf{R}\sqrt{d_r}\mathbf{L}_r\mathrm{e}^{i\omega t}}{m_j} \tag{29}$$

in which ξ_j is the damping ratio of OCL. m_j is the jth diagonal element in the matrix $\tilde{\mathbf{M}}_{\mathrm{T}}^{\mathrm{G}}$. $\eta_{r,j}$ is the rth harmonic generalised pseudo-displacement response excited by the rth harmonic generalised pseudo-wind excitation. According to the principle of PEM, the steady-state response can be calculated by

$$\mathbf{U}_{r,j}=\phi_j\eta_{r,j}=\frac{\phi_j\mathbf{H}_j\left(\omega\right)\phi_j^{\mathrm{T}}\mathbf{R}\sqrt{d_r}\mathbf{L}_r\mathrm{e}^{i\omega t}}{m_j} \tag{30}$$

in which,

$$\mathbf{H}_j\left(\omega\right)=\frac{1}{\omega_j^2-\omega^2+2i\xi_j\omega_j\omega} \tag{31}$$

The spectral matrix $\mathbf{S}_{\mathrm{uu}}^{j}$ of OCL response at jth mode can be expressed by

$$\mathbf{S}_{\mathrm{uu}}^{j}=\sum_{r=1}^{N_{\mathrm{r}}}\mathbf{U}_{r,j}^{*}\mathbf{U}_{r,j}^{\mathrm{T}} \tag{32}$$

in which N_{r} is the column number of the matrix $\mathbf{L}$. In this way, the variance of the OCL response can be estimated by the summation of $\mathbf{S}_{\mathrm{uu}}^{j}$ of each mode.

V. Analysis of Resulting Wind Deflection

In this section, a ten-span OCL constructed using the parameters of the reference model in the benchmark [31] is taken as the analysis objective. The contact line aerodynamic coefficients C_{L} and C_{D} are obtained through the wind tunnel experiment in [39]. The cross-sections of messenger line and droppers are assumed as a circular section, of which the drag coefficient is close to 1 and the lift can be neglected. The steady wind speeds are chosen as 10 m/s, 20 m/s, 30 m/s and 40 m/s in the following analysis. The wind speed of 40 m/s is a bit higher than the normal maximum wind speed according to [40].

A. Static wind deflection analysis

Considering an extreme condition, when the wind speed is 40 m/s, the resulting configuration of the OCL is presented in Fig .6 (a). It is seen that the strong wind causes a significant deflection of the OCL relative to its original configuration. The

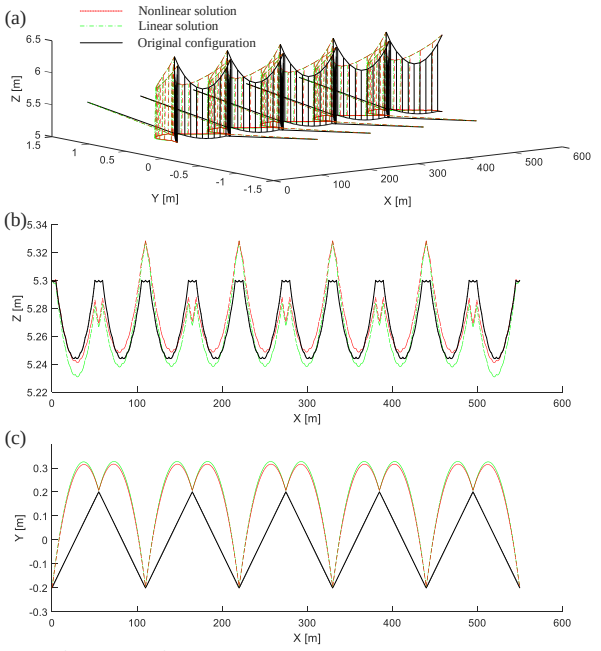

Fig. 6. Configuration of OCL with 40 m/s wind speed: (a) golabl view; (b) side view of contact line; (c) top view of contact line

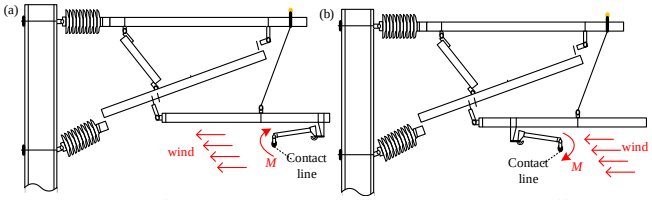

Fig. 7. Two types of cantilever: (a) Push-off cantilever; (b) pull-off cantilever

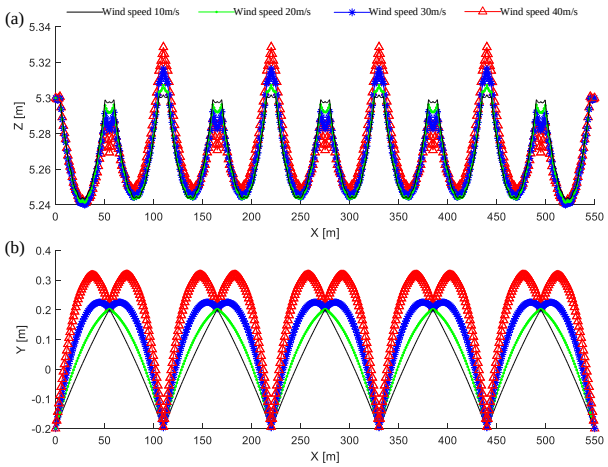

Fig. 8. Static contact line deflection at different wind speed: (a) side view; (b) top view

side view of the contact line is presented in Fig. 6 (b). Due to the existence of stagger, the steady arm shows opposite deflections in adjacent two spans. The maximum uplift occurs at around the steady arm point, which reaches about 28 mm. The contact line has a positive peak at around odd steady arms but has a negative peak at around even steady arms. This phenomenon can be explained by the structures of two types of cantilever as shown in Fig. 7. For the analysis object, the OCL has a push-off cantilever at the odd supports while it has a pull-off cantilever at the even supports. When the push-off cantilever is subjected to a crosswind, an uplift of the contact line at the end of the steady arm can be caused. For the pull-off cantilever, as shown in Fig. 7 (b), a decline of the contact line at the end of the steady arm can be caused. It is also seen that the linear solution results in significant errors when evaluating the vertical uplift. The errors can be ascribed to the non-smooth nonlinearity of droppers, which plays an important role in affecting the vertical behaviour of OCL. In contrast, the linear and nonlinear solutions present a small difference in evaluating the lateral deflection, as shown in Fig. 6 (c). The nonlinearity of the lateral OCL vibration is only caused by the geometrical nonlinearity of the messenger and contact lines, which is insignificant compared with the non-smooth nonlinearity of droppers. The nonlinear solutions for the static contact line deflections at different speeds are presented in Fig. 8. In Fig. 8 (a), it is seen that the increase of steady wind causes a significant increase of the uplift at the support, but does not largely affect the displacement in the middle span. The contact line at the support has lower elasticity than the middle span, which is more sensitive to the wind load. When the wind speed is over 30 m/s, the maximum lateral deflection is outside of the stagger (±0.2 m). Normally the lateral safe working range is ±

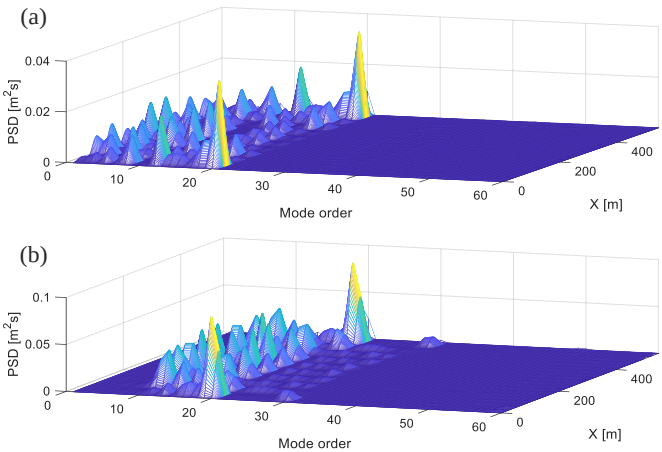

Fig. 9. PSD of contact line deflection versus mode order at different positions: (a) lateral vibration; (b) vertical vibration

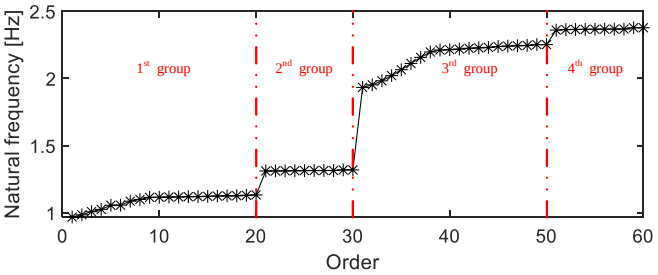

Fig. 10. OCL natural frequencies versus mode order

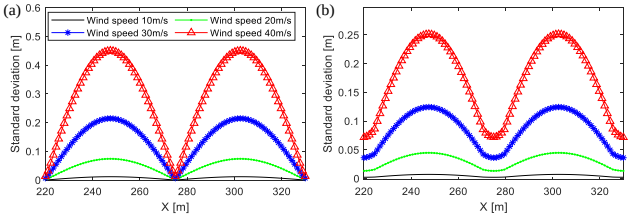

Fig. 11. Standard deviations of contact line displacement with different wind speeds: (a) Lateral vibration; (b) Vertical vibration

0.6 m for the widely-used pantograph in the world [3]. The lateral static wind deflection of the contact line is still within the safety range even at 40 m/s steady wind speed.

B. Buffeting analysis

The previous research on OCL damping [41] indicates that the OCL is a lightly damped system and its damping ratio is normally within 0.0005-0.002. The damping ratio is set as 0.001 in this analysis to investigate the buffeting behaviour. According to Eq. (23), the response of OCL buffeting can be seen as the summation of the contribution of first q modes. The mode number q must be determined firstly. When the wind speed is 40 m/s, the PSDs of the contact line displacement along the longitudinal direction are presented in Fig. 9. The first 20 modes have the dominant contribution to the buffeting of OCL. Normally the OCL is fixed at the endpoints. The boundary conditions of the end spans are different from that of the central spans. That is why the shapes in end spans are a bit different from the central spans, especially at 20th mode. The first 60 orders of OCL natural frequency are presented in Fig. 10. It is seen that the first group contains the first 20 natural frequencies of the OCL. In combination with the analysis of Fig. 8, the OCL

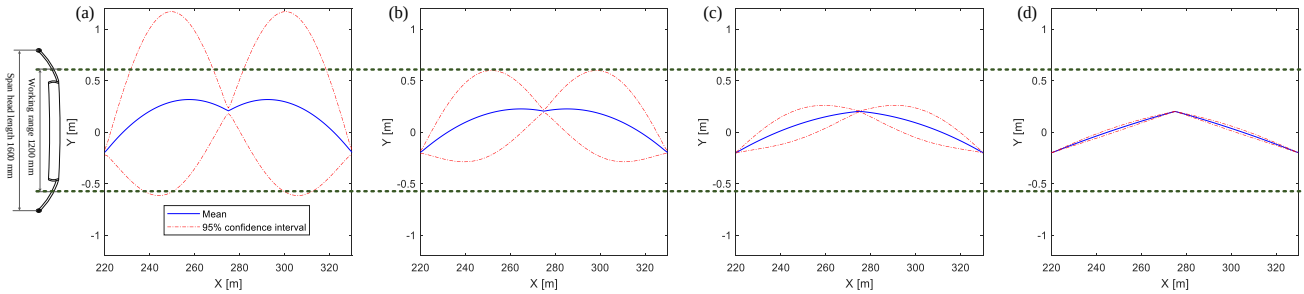

Fig. 12. Wind deflection of OCL with 95% confidence interval: (a) wind speed 40 m/s; (b) wind speed 30 m/s; (c) wind speed 20 m/s; (d) wind speed 10 m/s;

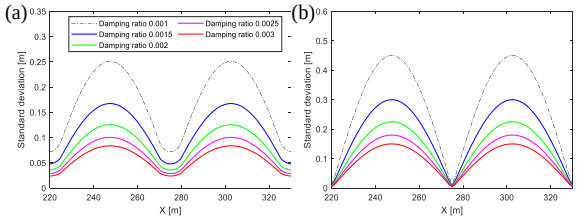

Fig. 13. Standard deviations of contact line displacement with different damping ratios: (a) Vertical vibration; (b) Lateral vibration

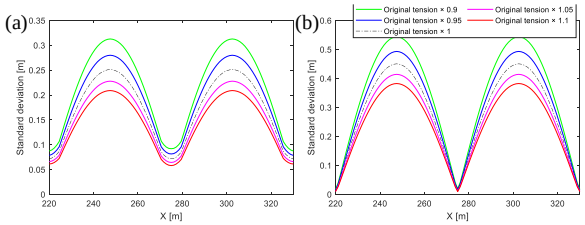

Fig. 14. Standard deviations of contact line displacement with different tensions: (a) Vertical vibration; (b) Lateral vibration

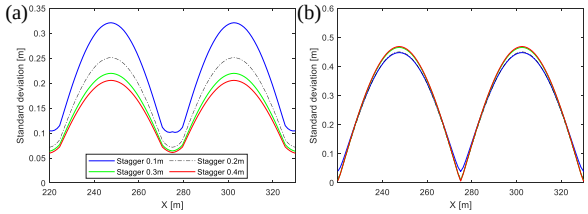

Fig. 15. Standard deviations of contact line displacement with different staggers: (a) Vertical vibration; (b) Lateral vibration

buffeting is dominated by the first group of modes and the contribution of higher modes can be neglected. To be cautious, the first and second groups (namely first 30 modes) are selected to calculate the OCL buffeting response in this analysis.

As the OCL is a periodical structure, only the two central spans are selected as the analysis object. The standard deviations of contact line displacement at different wind speeds are presented in Fig. 11. It is seen that the increase of wind speed causes a sharp increase in the fluctuation of contact line vibration. Particularly, when the wind speed is 40 m/s, the standard deviation of lateral contact line displacement at mid-span point reaches 0.45 m, which is 38.3 times larger than the value at 10 m/s wind speed. The results highly suggest that the lateral displacement of the contact line should be assessed in the design stage to guarantee that the contact line is always within the safe range of the pantograph head. Taking the effect of both steady and fluctuating winds, the lateral wind deflections with a confidence interval of 95% at different wind speeds are presented in Fig. 12. Considering a typical pantograph with 1.2 m working length [3], the risk of dewirement at each wind speed can be evaluated. When only the steady wind is considered, the contact line is always within the working range of the pantograph. However, when the fluctuating wind is also included, the contact line is outside the pantograph working range at 40 m/s wind speed. The maximum deflection occurs at around the mid-span point, which may lead to a risk of dewirement and damage the pantograph. This analysis suggests that the allowed maximum wind speed for the given pantograph-OCL system should be lower than 30 m/s. Otherwise, an optimisation is needed to improve the wind-resistance capability of OCL. However, it should be noted that the pantograph position can be moved by the wind load in real life. The analysis of Fig. 12 only provides conservative results. In the next section, the effect of some key parameters on the buffeting is discussed to facilitate the optimisation of OCL subjected to strong wind loads.

VI. Effect of Key Parameters on Buffeting

Understanding the effect of key parameters on OCL buffeting is essential for the design and optimisation of OCL in strong wind field. In this section, the sensitivities of the damping ratio, the tension and the stagger to the buffeting is analysed.

A. Effect of damping ratio

The field test results show that the damping ratio of OCL associated with the first group of natural frequency is around 0.001-0.0015 [41]. The current standard specifies that the damping ratio of OCL can be chosen from the range of 0.0005-0.002 [42]. In this analysis, the damping ratio range is defined as 0.001-0.003. Considering a 40 m/s wind speed, the standard deviation of contact line displacement versus the damping ratio is presented in Fig. 13. It is seen that the increase of damping ratio can effectively reduce the fluctuation of contact line buffeting. For both of the vertical and lateral vibrations, the maximum standard deviation of contact line displacement decreases by 66.67% when the damping ratio increases from 0.001 to 0.003. Considering a 95% confidence interval, the OCL contact line is within the working range of the pantograph head when the damping ratio is over 0.002. It is suggested that some damping components should be added to suppress the OCL wind deflection in strong wind field.

B. Effect of tension

The tension class directly determines the design speed a OCL. In this sub-section, the tensions on both messenger and contact lines are changed to 0.9, 0.95, 1.05 and 1.1 times of the original

tension to evaluate the OCL wind deflection with different tension classes. The standard deviation of the contact line displacement versus the tension is presented in Fig. 14. It is seen that the increase of the tension has some positive effect on the reduction of the buffeting. The maximum standard deviation of contact line displacement decreases by 33.22% when the tension increases from 0.9 to 1.1 times of the original value.

C. Effect of stagger

The stagger of OCL is set to reduce the wear on the pantograph strip. In this sub-section, the OCL stagger is set from 0.1 to 0.4 to calculate the OCL wind deflection. The standard deviation of the contact line displacement versus the stagger is presented in Fig. 15. It is seen that the increase of stagger can reduce the vertical vibration fluctuation caused by the stochastic wind, but has no significant effect on the lateral vibration. This finding is consistent with the time-domain analysis reported in [26]. For a good current collection quality, a larger stagger is desired to reduce the negative effect of the stochastic wind on the contact force. But a large stagger has no contribution to the lateral vibration, in contrast, it may increase the risk of dewirement.

VII. Conclusions

This paper presents a response spectrum analysis of OCL wind deflection caused by both of the steady and fluctuating winds. The main conclusions can be summarised as follows:

1) The dropper slackness has a significant effect on the OCL vertical deflection caused by a steady wind. A nonlinear procedure is desired to calculate the vertical wind deflection of OCL.

2) The OCL buffeting is dominated by the first group of OCL modes while the contribution of higher modes can be neglected.

3) The contact line is always within the safe working range of the pantograph head when only the steady wind load is considered. However, the stochastic wind load causes non-negligible fluctuation of OCL. The contact line may be outside of the pantograph working range in a strong stochastic wind field.

4) The OCL buffeting can be effectively suppressed by the increase of the damping ratio and the OCL tension. The increase of stagger has a positive effect on vertical vibration but has no significant contribution to suppressing the lateral vibration.

One shortcoming of the response spectrum analysis method is that the vertical dropper slackness and the interaction with pantographs cannot be considered. The Monte Carlo method will be implemented to evaluate the dispersion and distribution of contact forces of pantograph-OCL in the future.

Acknowledgement

This work was supported in part by the National Natural Science Foundation of China (U1734202).

References

[1] M. Zhang, F. Xu, and Y. Han, “Assessment of wind-induced nonlinear post-critical performance of bridge decks,” *J. Wind Eng. Ind. Aerodyn.*, vol. 203, 2020, doi: 10.1016/j.jweia.2020.104251.

[2] M. Zhang, F. Xu, and O. Øiseth, “Aerodynamic damping models for vortex-induced vibration of a rectangular 4:1 cylinder: Comparison of modeling schemes,” *J. Wind Eng. Ind. Aerodyn.*, vol. 205, 2020, doi: 10.1016/j.jweia.2020.104321.

[3] *EN 50119. Railway applications — Fixed installations — Electric traction overhead contact lines. 2015*. 2015.

[4] Y. Song, Z. Liu, H. Wang, X. Lu, and J. Zhang, “Nonlinear analysis of wind-induced vibration of high-speed railway catenary and its influence on pantograph–catenary interaction,” *Veh. Syst. Dyn.*, vol. 54, no. 6, pp. 723–747, 2016, doi: 10.1080/00423114.2016.1156134.

[5] Z. Liu, Y. Song, Y. Han, H. Wang, J. Zhang, and Z. Han, “Advances of research on high-speed railway catenary,” *J. Mod. Transp.*, vol. 26, no. 1, pp. 1–23, Mar. 2018, doi: 10.1007/s40534-017-0148-4.

[6] S. H. Kia, F. Bartolini, A. Mpanda-Mabwe, and R. Ceschi, “Pantograph-catenary interaction model comparison,” *IECON Proc. (Industrial Electron. Conf.*, pp. 1584–1589, 2010, doi: 10.1109/IECON.2010.5675448.

[7] Y. Song, A. Rønnquist, and P. Nåvik, “Assessment of the High-Frequency Response in Railway Pantograph-Catenary Interaction Based on Numerical Simulation,” *IEEE Trans. Veh. Technol.*, vol. 69, no. 10, pp. 10596–10605, 2020, doi: 10.1109/TVT.2020.3015044.

[8] Z. Xu, G. Gao, Z. Yang, W. Wei, and G. Wu, “An Online Monitoring Device for Pantograph Catenary Arc Temperature Detect Based on Atomic Emission Spectroscopy,” *ICHVE 2018 - 2018 IEEE Int. Conf. High Volt. Eng. Appl.*, pp. 1–4, 2019, doi: 10.1109/ICHVE.2018.8641866.

[9] P. Boffi *et al.*, “Optical fiber sensors to measure collector performance in the pantograph-catenary interaction,” in *IEEE Sensors Journal*, Jun. 2009, vol. 9, no. 6, pp. 635–640, doi: 10.1109/JSEN.2009.2020244.

[10] H. Wang, A. Núñez, Z. Liu, Y. Song, F. Duan, and R. Dollevoet, “Analysis of the evolvement of contact wire wear irregularity in railway catenary based on historical data,” *Veh. Syst. Dyn.*, vol. 56, no. 8, pp. 1207–1232, 2018, doi: 10.1080/00423114.2017.1408919.

[11] T. Jiang, G. T. Frøseth, A. Rønnquist, and E. Fagerholt, “A robust line-tracking photogrammetry method for uplift measurements of railway catenary systems in noisy backgrounds,” *Mech. Syst. Signal Process.*, vol. 144, 2020, doi: 10.1016/j.ymssp.2020.106888.

[12] W. Liu, Z. Liu, Q. Li, Z. Han, and A. Nunez, “High-Precision Detection Method for Structure Parameters of Catenary Cantilever Devices using 3D Point Cloud Data,” *IEEE Trans. Instrum. Meas.*, pp. 1–1, Dec. 2020, doi: 10.1109/tim.2020.3045801.

[13] Y. Song, P. Antunes, J. Pombo, and Z. Liu, “A methodology to study high-speed pantograph-catenary interaction with realistic contact wire irregularities,” *Mech. Mach. Theory*, vol. 152, no. xxxx, p. 103940, May 2020, doi: 10.1016/j.mechmachtheory.2020.103940.

[14] B. Allotta, L. Pugi, and F. Bartolini, “Design and experimental results of an active suspension system for a high-speed pantograph,” *IEEE/ASME Trans. Mechatronics*, vol. 13, no. 5, pp. 548–557, Oct. 2008, doi: 10.1109/TMECH.2008.2002145.

[15] T. X. Wu and M. J. Brennan, “Dynamic stiffness of a railway overhead wire system and its effect on pantograph-catenary system dynamics,” *J. Sound Vib.*, vol. 219, no. 3, pp. 483–502, 1999, doi: 10.1006/jsvi.1998.1869.

[16] Y. Song, Z. Liu, F. Duan, Z. Xu, and X. Lu, “Wave propagation analysis in high-speed railway catenary system subjected to a moving pantograph,” *Appl. Math. Model.*, vol. 59, pp. 20–38, 2018, doi: 10.1016/j.apm.2018.01.001.

[17] B. Sun, W. Krieger, M. Rohwerder, D. Ponge, and D. Raabe, “Dependence of hydrogen embrittlement mechanisms on microstructure-driven hydrogen distribution in medium Mn steels,” *Acta Mater.*, vol. 183, pp. 313–328, 2020, doi: 10.1016/j.actamat.2019.11.029.

[18] J. Zhang, W. Liu, K. Qiao, M. Yu, T. Wang, and Z. Yang, “Influence of catenary tension on static elasticity and dynamic contact force between pantograph and catenary,” *IET Electr. Syst. Transp.*, vol. 7, no. 3, pp. 201–206, Sep. 2017, doi: 10.1049/iet-est.2016.0076.

[19] Z. Qu, S. Yuan, R. Chi, L. Chang, and L. Zhao, “Genetic optimization method of pantograph and catenary comprehensive monitor status prediction model based on adadelta deep neural network,” *IEEE Access*, vol. 7, pp. 23210–23221, 2019, doi: 10.1109/ACCESS.2019.2899074.

[20] Z. Xu, Y. Song, and Z. Liu, “Effective Measures to Improve Current Collection Quality for Double Pantographs and Catenary Based on Wave Propagation Analysis,” *IEEE Trans. Veh. Technol.*, vol. 69, no.

6, pp. 6299–6309, 2020, doi: 10.1109/TVT.2020.2985382.
[21] Y. Song, Z. Wang, Z. Liu, and R. Wang, "A spatial coupling model to study dynamic performance of pantograph-catenary with vehicle-track excitation," *Mech. Syst. Signal Process.*, vol. 151, p. 107336, 2021, doi: 10.1016/j.ymssp.2020.107336.
[22] Y. Song, Z. Liu, A. Ronnquist, P. Navik, and Z. Liu, "Contact Wire Irregularity Stochastics and Effect on High-Speed Railway Pantograph-Catenary Interactions," *IEEE Trans. Instrum. Meas.*, vol. 69, no. 10, pp. 8196–8206, Oct. 2020, doi: 10.1109/TIM.2020.2987457.
[23] Y. Song, Z. Liu, and X. Lu, "Dynamic Performance of High-Speed Railway Overhead Contact Line Interacting with Pantograph Considering Local Dropper Defect," *IEEE Trans. Veh. Technol.*, vol. 69, no. 6, pp. 5958–5967, 2020, doi: 10.1109/TVT.2020.2984060.
[24] Y. Song, Z. Liu, H. Wang, J. Zhang, X. Lu, and F. Duan, "Analysis of the galloping behaviour of an electrified railway overhead contact line using the non-linear finite element method," *Proc. Inst. Mech. Eng. Part F J. Rail Rapid Transit*, vol. 232, no. 10, pp. 2339–2352, 2018, doi: 10.1177/0954409718769751.
[25] M. T. Stickland, T. J. Scanlon, I. A. Craighead, and J. Fernandez, "An investigation into the mechanical damping characteristics of catenary contact wires and their," *Proc. Inst. Mech. Eng. Part F J. Rail Rapid Transit*, vol. 217, no. August 2000, pp. 63–72, 2001.
[26] Y. Song, Z. Liu, F. Duan, X. Lu, and H. Wang, "Study on wind-induced vibration behavior of railway catenary in spatial stochastic wind field based on nonlinear finite element procedure," *J. Vib. Acoust. Trans. ASME*, vol. 140, no. 1, pp. 011010-1–14, 2018, doi: 10.1115/1.4037521.
[27] Z. Wang, Y. Song, Z. Yin, R. Wang, and W. Zhang, "Random Response Analysis of Axle-Box Bearing of a High-Speed Train Excited by Crosswinds and Track Irregularities," *IEEE Trans. Veh. Technol.*, vol. 68, no. 11, pp. 10607–10617, 2019, doi: 10.1109/TVT.2019.2943376.
[28] E. Muljadi, V. Gevorgian, M. Singh, and S. Santoso, "Understanding inertial and frequency response of wind power plants," 2012, doi: 10.1109/PEMWA.2012.6316361.
[29] Q. S. Li, Y. Q. Xiao, C. K. Wong, and A. P. Jeary, "Field measurements of typhoon effects on a super tall building," *Eng. Struct.*, vol. 26, no. 2, pp. 233–244, 2004, doi: 10.1016/j.engstruct.2003.09.013.
[30] J. H. Lin, Y. H. Zhang, and Y. Zhao, "Pseudo Excitation Method and some recent developments," in *Procedia Engineering*, 2011, vol. 14, pp. 2453–2458, doi: 10.1016/j.proeng.2011.07.308.
[31] S. Bruni *et al.*, "The results of the pantograph-catenary interaction benchmark," *Veh. Syst. Dyn.*, vol. 53, no. 3, pp. 412–435, Mar. 2015, doi: 10.1080/00423114.2014.953183.
[32] Y. Song, Z. Liu, Z. Xu, and J. Zhang, "Developed moving mesh method for high-speed railway pantograph-catenary interaction based on nonlinear finite element procedure," *Int. J. Rail Transp.*, vol. 7, no. 3, 2019, doi: 10.1080/23248378.2018.1532330.
[33] J. C. Kaimal, J. C. Wyngaard, Y. Izumi, and O. R. Coté, "Spectral characteristics of surface-layer turbulence," *Q. J. R. Meteorol. Soc.*, vol. 98, no. 417, pp. 563–589, 1972, doi: 10.1002/qj.49709841707.
[34] H. A. Panofsky and R. A. McCormick, "The spectrum of vertical velocity near the surface," *Q. J. R. Meteorol. Soc.*, vol. 86, no. 370, pp. 495–503, 1960, doi: 10.1002/qj.49708637006.
[35] H. W. Tieleman, "Universality of velocity spectra," *J. Wind Eng. Ind. Aerodyn.*, vol. 56, no. 1, pp. 55–69, 1995, doi: 10.1016/0167-6105(94)00011-2.
[36] H. W. Tieleman, "Roughness estimation for wind-load simulation experiments," *J. Wind Eng. Ind. Aerodyn.*, vol. 91, no. 9, pp. 1163–1173, 2003, doi: 10.1016/S0167-6105(03)00058-8.
[37] P. S. Veers, "Three-dimensional wind simulation.," 1988.
[38] Y. L. Xu, W. S. Zhang, J. M. Ko, and J. H. Lin, "Pseudo-excitation method for vibration analysis of wind-excited structures," *J. Wind Eng. Ind. Aerodyn.*, vol. 83, no. 1–3, pp. 443–454, 1999, doi: 10.1016/S0167-6105(99)00092-6.
[39] A. R. Elvebakken, "Estimation of Aerodynamic Forces on a Railway Contact Wire and Their Effect on Galloping Instability-Wind Tunnel Testing of an AC-120 Contact Wire." NTNU, 2018.
[40] F. Kiessling, R. Puschmann, A. Schmieder, and E. Schneider, *Contact lines for electric railways, third edition*, Third Edit., vol. 116, no. 3. John Wiley & Sons, 2018.
[41] D. Zou, W. H. Zhang, R. P. Li, N. Zhou, and G. M. Mei, "Determining damping characteristics of railway-overhead-wire system for finite-element analysis," *Veh. Syst. Dyn.*, vol. 54, no. 7, pp. 902–917, 2016, doi: 10.1080/00423114.2016.1172715.
[42] EN 50367. *Railway applications — Current collection systems — Technical criteria for the interaction between pantograph and overhead line.*, no. August 2013.

Yang Song (Member, IEEE) received the Ph.D. degree from Southwest Jiaotong University, Sichuan, China, in 2018. He worked as a Research Fellow with the Institute of Railway Research, University of Huddersfield, U.K. from October 2018 to September 2019. He is currently a Postdoctoral Researcher with the Department of Structural Engineering, Norwegian University of Science and Technology, Norway. His research interests involve the assessment of railway pantograph-OCL interactions, the wind-induced vibration of long-span structures in railway transportation.

Mingjie Zhang received his Ph.D. degree from Dalian University of Technology, Dalian, China, in 2019. He is currently a Postdoctoral Researcher at the Department of Structural Engineering, Norwegian University of Science and Technology, Norway. His research interests involve the flow-induced vibration of various structures and the structural dynamics of highway and railway transportations.

Hongrui Wang (Member, IEEE) received his Ph.D. degree from the Section of Railway Engineering, Delft University of Technology, Delft, The Netherlands, in 2019, where he was a Postdoctoral Researcher until November 2020. He is currently an Assistant Professor with the Section of Railway Engineering, Delft University of Technology. He is an Associate Editor for the journal IEEE Transactions on Instrumentation and Measurement. His research interests include signal processing, artificial intelligence, and their applications in the structural health monitoring and digital modelling and design of railway infrastructures.